Spiral Photonic Crystal Fiber-Based Dual-Polarized Surface Plasmon Resonance Biosensor

Md. Rabiul Hasan, *Student Member, IEEE*, Sanjida Akter, Ahmmed A. Rifat, Sohel Rana, Kawsar Ahmed, Rajib Ahmed, Harish Subbaraman, *Member, IEEE*, and Derek Abbott, *Fellow, IEEE*

Abstract—We numerically demonstrate a surface plasmon resonance biosensor-based on dual-polarized spiral photonic crystal fiber (PCF). Chemically stable gold material is used as the active plasmonic material, which is placed on the outer layer of the PCF to facilitate practical fabrication. Finite-element method-based numerical investigations show that the proposed biosensor shows maximum wavelength sensitivity of 4600 and 4300 nm/RIU in *x*- and *y*-polarized modes at an analyte refractive index of 1.37. Moreover, for analyte refractive index ranging from 1.33 to 1.38, maximum amplitude sensitivities of 371.5 RIU^{-1} and 420.4 RIU^{-1} are obtained in *x*- and *y*-polarized modes, respectively. In addition, the effects of changing pitch, different air hole diameter of the PCF and thickness of the gold layer on the sensing performance are also investigated. Owing to high sensitivity, improved sensing resolution and appropriate linearity characteristics, the proposed dual-polarized spiral PCF can be implemented for the detection of biological analytes, organic chemicals, biomolecules, and other unknown analytes.

Index Terms—Finite element method, photonic biosensor, surface plasmon resonance, sensitivity, sensing resolution.

I. Introduction

THE study of surface plasmon resonance (SPR) has achieved considerable attention due to several promising applications including bioimaging [1], biosensing [2], chemical detection [3], food safely [4], and environmental monitoring [5]. Extensive research on SPR technology has led to successful implementation in optoelectronic devices such as optical tunable filters [6] and thin-film thickness monitoring [7]. The theoretical concept of surface plasmons (SPs) was introduced by Ritchie [8]. Using a similar concept, Otto [9] and Kretschmann [10] based sensing techniques have been developed. Kretschmann SPR sensors have been widely implemented due to their robust sensing performance. Unfortunately, such sensors are generally bulky and consist of moving mechanical components. Therefore, the option for miniaturization and optimization of the sensor for stand off sensing applications is limited. To effectively overcome the limitations of the conventional prism coupled (Kretschmann setup) sensors, optical fiber is substituted for the prism.

Optical fiber based SPR sensors offer a wider operating region and high sensing resolution [11]. However, these sensors are limited due to narrow acceptance angles. Recently, photonic crystal fibers (PCFs) have been extensively employed for SPR sensing. The PCF permits miniaturization of the sensor by taking advantage of its small physical dimension. Besides, guiding modes can be easily manipulated by varying the PCF's structural parameters (pitch, air-hole dimension, number of rings etc.), which eventually allows improved sensing performance [11]. The PCF SPR sensor operates based on the guided evanescent field. By properly designing the core-cladding geometry, it is possible to partially penetrate the evanescent field towards the metallic surface. This field strikes the metallic surface and stimulates the free electrons of the plasmonic metal. When the frequency of the guided evanescent fields is matched with the natural frequency of the surface electrons, a surface plasmon wave (SPW) is generated. This SPW propagates in the metal-dielectric interface [12]. This condition results in a resonance, at which a sharp loss peak is observed. An unknown sample (analyte) can be detected via the shifting of the resonant wavelength or the variation of the confinement loss peak.

Recently, most PCF based sensors have been explored using gold, silver, copper and aluminium in order to create SPR phenomenon [11]. From the optical point of view, silver can be regarded as the best plasmonic material due to no interband transition and low damping loss [13]. Unfortunately, in the presence of an aqueous solution a brittle oxide layer is formed, which effectively reduces the sensing performance. Aluminium is another potentially attractive plasmonic material having moderate damping loss and high electron density [13]. However, it is also affected by a similar oxidation issue. Many of the PCF based SPR sensors use gold as the active plasmonic material. Unlike other materials, gold is chemically inert and does not oxidize easily [14]. Besides, it is biocompatible and is easy to structure using existing fabrication technologies [14].

M. R. Hasan and S. Akter are with the Department of Electronics and Telecommunication Engineering, Rajshahi University of Engineering and Technology, Rajshahi, 6204, Bangladesh (e-mail: ruetrabu@gmail.com; sanjida.ruet11@gmail.com).

A. A. Rifat is with the Nonlinear Physics Centre, Research School of Physics and Engineering, Australian National University, Acton, ACT-2601, Australia (e-mail: rifatahmmed.aoni@anu.edu.au).

S. Rana and H. Subbaraman are with the Department of Electrical and Computer Engineering, Boise State University, Boise, ID 83725 USA (e-mail: sohelrana@u.boisestate.edu; harishsubbaraman@boisestate.edu).

K. Ahmed is with the Department of Information and Communication Technology, Mawlana Bhashani Science and Technology University, Santosh 1902, Bangladesh (e-mail: k.ahmed.bd@ieee.org).

R. Ahmed is with the School of Engineering, University of Birmingham, Birmingham B15 2TT, U.K. (e-mail: rxa448@student.bham.ac.uk).

D. Abbott is with the School of Electrical and Electronic Engineering, University of Adelaide, Adelaide, SA 5005, Australia (e-mail: derek.abbott@adelaide.edu.au).

Digital Object Identifier 10.1109/JSEN.2017.2769720

Various PCF based SPR sensors have been explored in the literature in order to improve the sensing performance by increasing sensitivity and sensor resolution [15]–[20]. Internal metal coating with selective liquid infiltration based sensors has been reported in [15]–[17]. However, realizing uniform metal coating thickness of several inner air holes is difficult in practice. To overcome the limitations of such sensors, various forms of D-shaped PCF sensors have been proposed [18]–[20]. Although D-shaped PCF sensors provide good results in terms of sensitivity, they require additional surface polishing to obtain flat surface. In practice, it is a challenging task to accurately put out a predefined area of the PCF. In recent years, several PCF SPR sensors have been proposed, where both plasmonic material and the analyte are kept outside the PCF surface [21]–[24].

These types of sensors provide additional facility in practical sensing applications due to their straightforward design. Additionally, depositing the plasmonic material on the outer surface is easier compared to covering the inner air holes. To date, PCF structures have been investigated using this design criterion. A copper-graphene based PCF SPR sensor has been demonstrated in [21], where comparatively lower wavelength sensitivity of 2000 nm/RIU and amplitude sensitivity of 140 RIU^{-1} has been reported. The sensor proposed in [22] showed improved performance in terms of amplitude sensitivity and resolution. However, it contains air holes with four different diameters, which potentially limit its fabrication feasibility. Recently, another gold coating based PCF SPR sensor has been proposed showing sensitivities of 4000 nm/RIU and 320 RIU^{-1} in the narrow sensing range between 1.33 and 1.36 [23] Very recently, a circular PCF based SPR sensor has been demonstrated, where wavelength sensitivity of 2200 nm/RIU and amplitude sensitivity of 266 RIU^{-1} has been reported in the sensing range between 1.33–1.36 [24].

Apart from external metal coated PCF sensors, other types of sensors have been reported in the literature based on metal nanowire [25], microfluidic slots [26], tapered fiber [27], and multi-core flat fiber configurations [28]. However, practical implementation using such sensors is challenging since they are often required to selectively draw liquid into small air holes. In addition, these PCFs generally exhibit higher propagation loss since metal layers are selectively placed nearby the core. The loss is increased because of the attraction of core field by the plasmonic metal [11]. In practice, it is desirable to have low propagation loss since input optical power will be rapidly attenuated with high propagation loss. As a result, it is difficult to obtain measurable signal to detect an unknown sample. In microfluidic slotted PCF SPR sensors, a metal layer coating is deposited on the outer surface. To obtain such a slotted structure, it is required to split the thin layer into several segments but this is difficult in practice. Besides SPR technique, sensors based on other technologies including interferometer [29], [30], Bragg or long periodic grating [31], and resonant coupling [32] have been also explored in the literature. A Mach-Zehnder PCF interferometer based RI sensor demonstrated in [29] showed maximum wavelength sensitivity and resolution of 326 nm/RIU and 5.20×10^{-5} RIU, respectively. Moreover, using the same sensing technique, a high sensitivity of 300 RIU^{-1} and a high resolution of 3×10^{-6} RIU have been reported [30]. Very recently, Bragg gratings in surface-core fiber based RI sensor has been proposed with sensitivity of 40 nm/RIU and resolution of 2.5×10^{-4} RIU [31]. Based on the selectively resonant coupling microstructured-core PCF sensor has been introduced showing wavelength sensitivity and resolution of 8500 nm/RIU and 2.02×10^{-6} RIU, respectively [32].

In this paper, we propose a simple spiral PCF structure based SPR sensor to obtain high sensitivity and low-loss characteristics. The aim of this work is to numerically investigate the performance parameters. We mainly focus on the sensitivity analysis by varying several structural parameters of the sensor. The numerical investigation is performed in both x- and y-polarized modes in the wider refractive index (RI) sensing range from 1.33 to 1.38. The plasmonic material is deposited on the outermost layer of the PCF, which reduces the major fabrication challenges. Moreover, the detection process is more practical since an unknown liquid sample can be identified by flowing it over the outer surface. The effect of changing fiber design parameters such as pitch, air hole diameter and gold layer thickness is investigated to obtain the optimal sensing performance. Moreover, possible fabrication techniques to realize the proposed PCF and thin outer gold layer are also discussed thoroughly.

II. DESIGN AND THEORETICAL MODELING OF THE PROPOSED SPIRAL PCF SPR BIOSENSOR

The 2D cross section view of the proposed spiral PCF SPR sensor is shown in Fig. 1(a). The spiral PCF consists of six arms and three rings. The dashed lines connecting the holes are to illustrate how they form spiral trajectories. This is essentially an equiangular spiral PCF since a constant angle of 60 degree is retained between two air holes of a same ring. The successive angular displacement (θ) between air holes in the same spiral arm is 30 degrees. It should be mentioned that two air holes along the horizontal axis in the first ring are missing to create an asymmetry for birefringence. The birefringence leads to increased coupling between x- or y-polarized modes and the surface plasmon polariton (SPP) mode; thereby, enhancing the sensing performance. The center-to-center distance between the central and air hole of the first ring is denoted as the pitch, Λ. The distance from the central air hole to air holes of the second and third ring is $1.4 \times \Lambda$ and $1.8 \times \Lambda$, respectively. The diameter of the central air hole is $d_c = 0.2 \times \Lambda$. If we set d_c larger than this value it potentially reduces the effective mode index and eventually it will increase the confinement loss [23].

On the other hand, using a smaller value than $0.2 \times \Lambda$ would be difficult to fabricate. The two smaller air holes along the horizontal axis of the third ring is $d_1 = 0.3 \times \Lambda$. The target property is to increase the interaction of evanescent field with the sensing layer. With this in mind, two air holes are scaled down so that the guiding mode can easily reach to the metallic surface [24]. The diameter of remaining air holes of the PCF is $d = 0.65 \times \Lambda$. The background material is fused silica, whose RI is obtained from [28].
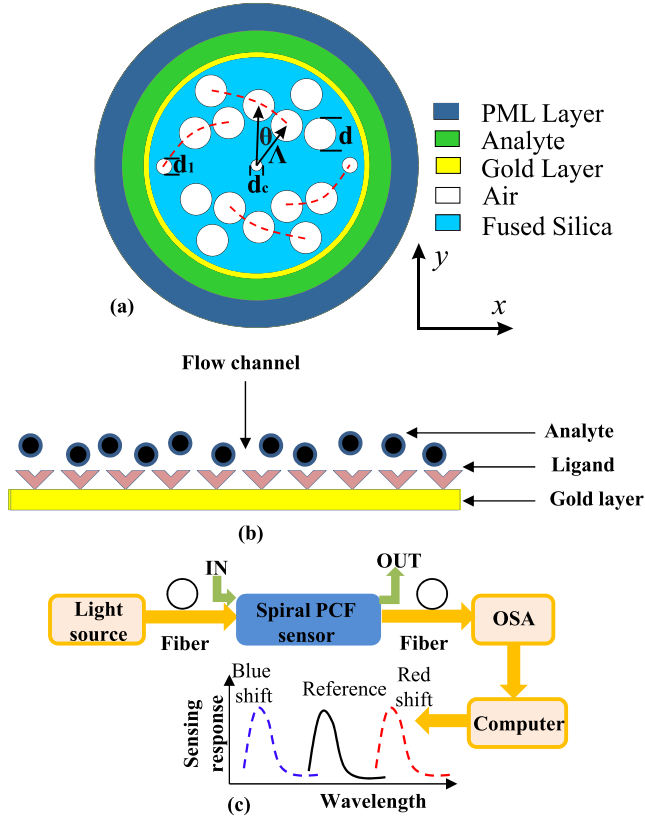
Fig. 1. (a) Design of the proposed spiral PCF sensor in 2D computational model. (b) Analyte flow through the sensing layer. (c) Basic setup for practical sensing with typical sensing response curve.

On the top of the PCF surface a thin gold layer coating is placed, which is denoted as t_g. The dielectric function of gold material can be obtained using the Drude-Lorentz model [33],

$$\varepsilon_{Au} = \varepsilon_\infty - \frac{\omega_D^2}{\omega(\omega + j\gamma_D)} - \frac{\Delta\varepsilon.\Omega_L^2}{(\omega^2 - \Omega_L^2) + j\Gamma_L\omega} \quad (1)$$

where ε_∞ is the permittivity at high frequency having the value of 5.9673. Here, ω_D and γ_D are the plasma frequency and the damping frequency, respectively. Note that, other parameters in the model are $\omega_D/2\pi = 2113.6$ THz, $\gamma_D/2\pi = 15.92$ THz and $\Delta\varepsilon = 1.09$. Also, the spectral width is $\Gamma_L/2\pi = 104.86$ THz and the oscillator strength is $\Omega_L/2\pi = 650.07$ THz, respectively.

An analyte layer is used on the top of the gold layer, which acts as the sensing medium. The thickness of the analyte layer is 1.8 μm. The analyte layer thickness is chosen after performing the convergence test, which confirms better accuracy of the simulation results. We changed analyte layer thickness from 0.25 μm to 15 μm. We found that increasing analyte layer thickness results extremely small change of imaginary part of the effective index, Im (n_{eff}), after 1.5 μm. Such insignificant change does not affect the convergence test result. Although larger thickness of the analyte layer could be used, it would unexpectedly lengthen the simulation time. Therefore, optimal analyte layer thickness of 1.8 μm was used in order to maintain a balance between simulation speed and accuracy of the simulation results. The outermost layer is the perfectly match layer (PML) having the thickness of 2 μm.

In the simulation, we used finer meshing elements. Besides, finer meshing elements are adequate to precisely investigate the mode profile.

The design and simulation of the spiral PCF SPR sensor has been performed using the commercially available state-of-the-art *COMSOL 5.2* software. The computational domain took 41,176 triangular elements, 2140 edge elements, and 181.4 μm^2 mesh area to represent the proposed model. Throughout the simulation, we have used $\Lambda = 2$ μm, $d_c = 0.4$ μm, $d_1 = 0.6$ μm, $d = 1.3$ μm and $t_g = 30$ nm unless otherwise stated. The diameter of the PCF is about 8 μm.

Although this is basically a simulation based analysis, the generalized sensing setup using the proposed sensor is shown in Fig. 1 (c). A broadband/monochromatic light source can be used to lunch the optical power into a conventional single mode fiber (SMF). A splicing technique can be used to connect the SMF with the proposed PCF sensor. On the top the gold surface a sample analyte channel can be assumed as illustrated in Fig. 1(b), where IN and OUT of the sample can be preserved through a pump. The effective refractive index (n_{eff}) of the SPP mode will be changed because of the interaction of sample analyte with the ligand; thereby either blue or red shift will occur. The optical spectrum analyser (OSA) or photodetector can be used to measure the transmitted light. The output the OSA or photodetector can be used for further observation on a computer display.

III. SIMULATION RESULTS AND DISCUSSIONS OF THE PROPOSED SPIRAL PCF SPR BIOSENSOR

The function of a biosensor is to detect biological and biochemical analytes by sensing their refractive index. In general, biological and biochemical interactions occur between refractive index ranges from 1.33 to 1.36 [11], [34]. The refractive index of the outer medium in the simulation model implicitly defines an analyte to be detected. The evanescent field originating from the propagating core-guided mode plays a prominent contribution in PCF SPR sensors. The guided evanescent field hits the metal surface and excites free electrons resulting in surface plasmon waves. Fundamental mode field distribution of the x-polarized core mode, y-polarized core mode, x-polarized SPP mode and y-polarized SPP mode are depicted in Fig. 2(a), (b), (c), and (d) with analyte RI of 1.36 and operating wavelength of 0.7 μm. The dispersion relationship is analyzed considering all materials involved in the design including silica, gold and outer analyte medium, which is shown in Fig. 2(e). It is clearly visible that the n_{eff} of the fundamental mode and refractive index of SPP mode coincides at wavelength of 0.70 μm.

This is known as the resonance wavelength, at which maximum energy will be transferred from the guided mode to the SPP mode. The coupling strength depends on which mode has closer interaction with the plasmon. Depending on the geometry of the PCF evanescent field of the x-polarized and y-polarized mode varies. Due to birefringence, the fundamental x-polarized and y-polarized mode displays different Im(n_{eff}). In the proposed design, x-polarized mode is tightly bound by the core resulting lower penetration of

Fig. 3. Loss spectrum with the variation of analyte RI from 1.33 to 1.38 for (a) x-polarized mode and (b) y-polarized mode. The fiber design parameters are set to: $\Lambda = 2$ μm, $d_c = 0.4$ μm, $d_1 = 0.6$ μm, $d = 1.3$ μm and $t_g = 30$ nm.
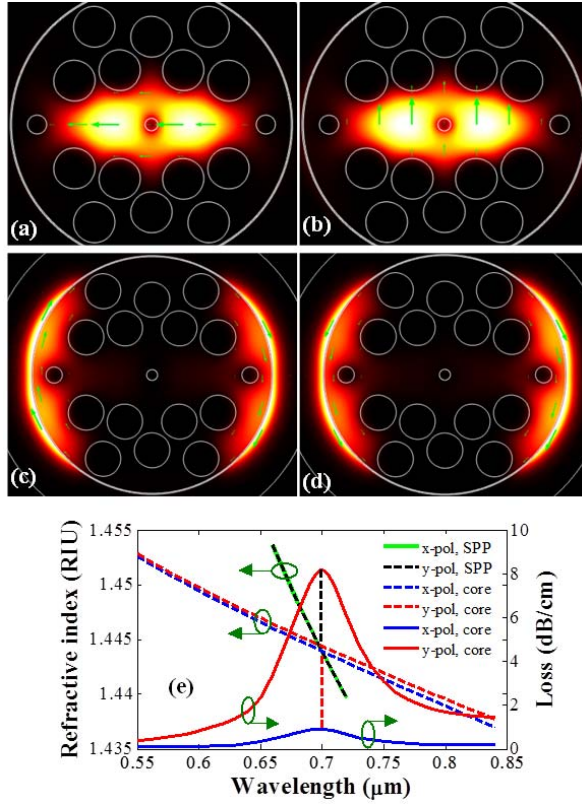

Fig. 2. Fundamental mode field profile of (a) x-polarized core mode, (b) y-polarized core mode, (c) x-polarized SPP mode, (d) y-polarized SPP mode at analyte RI of 1.36 and $\lambda = 0.70$ μm, and (e) dispersion relation of plasmonic mode, fundamental core mode and loss spectra for $t_g = 40$ nm and $n_a = 1.36$.

evanescent field. On the other hand, the y-polarized mode is loosely bound by the core yielding a comparatively higher evanescent field. As a result, the y-polarized mode shows higher coupling strength than that of the x-polarized mode, which is illustrated in Fig. 2(e). In our analysis, we have considered the effect of both x- and y- polarized modes.

Confinement loss is a key parameter in PCF based SPR biosensor. This loss can be calculated from the following expression [22]–[24],

$$\alpha(\text{dB/cm}) = 8.686 \times k_0 \text{Im}(n_{eff}) \times 10^4 \qquad (2)$$

where $k_0 = 2\pi/\lambda$ is the propagation constant in free space, λ is the wavelength in microns, and $\text{Im}(n_{eff})$ is the imaginary part of the n_{eff}.

The SPP mode is extremely sensitive to the RI of the sensing medium, which is a dielectric surface. In general, the n_{eff} of the SPP mode is strongly influenced by the small change of the liquid sample RI. As a result, the loss peak shifts correspondingly. The variation of loss depth with changing analyte RI from 1.33 to 1.38 is shown in Fig. 3 for x- and y-polarized modes, respectively. With analyte RI of 1.33, the phase matching point occurs at a wavelength of 0.58 μm for both x- and y-polarized modes. The corresponding loss depths are 0.5034 dB/cm and 4.04 dB/cm.

In practice, length of the sensor is restricted by the high propagation loss. Due to low propagation loss of the proposed fiber, a longer fiber can be utilized in practical sensing
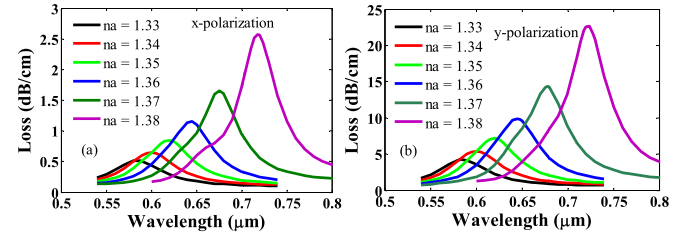
applications [32]. Moreover, splicing and alignment issues can be avoided, which effectively enhances the sensing performance [11]. It can be noticed that incrementing the analyte RI from 1.33 to 1.38 (with step size of 0.01) causes a monotonic increase of the peak loss depth. This is due to the fact that as analyte RI increases, the index difference between core and SPP mode becomes smaller, resulting significant change of confinement loss. Besides, indication of a red shift is observed i.e. incrementing the analyte RI changes the phase matching point towards higher wavelengths. For x- and y-polarized modes, the maximum loss depth is 2.58 dB/cm and 22.63 dB/cm with an analyte RI of 1.38 at a wavelength of 0.724 um. Higher loss depth leads to improved confinement of the guided mode, which enhances the field penetration through the cladding region. As a result, interaction with analyte increases and higher exchange of energy occurs from fundamental mode to the SPP mode.

In wavelength interrogation method, the sensitivity of a sensor depends on the maximum resonance wavelength shift. Using the wavelength interrogation method, the sensitivity can be expressed as [21],

$$S_\lambda(\text{nm/RIU}) = \Delta\lambda_{\text{peak}}/\Delta n_a \qquad (3)$$

where $\Delta\lambda_{\text{peak}}$ is the peak wavelength shift due to any change of analyte RI and Δn_a is the change of the two successive analyte RI. The proposed sensor shows resonance wavelength shift of 20, 20, 25, 30 and 43 nm in x-polarized mode with analyte RI varied from 1.33 to 1.34, 1.34 to 1.35, 1.35 to 1.36, 1.36 to 1.37 and 1.37 to 1.38, respectively. Therefore, according to Eq. 3 the theoretical wavelength sensitivities are 2000, 2000, 2500, 3000, and 4300 nm/RIU, respectively. On the other hand, for the same RI variations the wavelength shift are 20, 20, 25, 33 and 46 nm in y-polarized mode, which show wavelength sensitivities of 2000, 2000, 2500, 3300, and 4600 nm/RIU, respectively.

Resolution is another significant parameter that indicates the performance of a sensor. Using wavelength interrogation method, the resolution can be expressed by [28],

$$R(\text{RIU}) = \Delta n_a \times \Delta\lambda_{\text{min}}/\Delta\lambda_{\text{peak}} \qquad (4)$$

where $\Delta\lambda_{\text{min}}$ is the minimum spectral resolution and $\Delta\lambda_{\text{peak}}$ is the resonant wavelength shift. Assuming that $\Delta\lambda_{\text{min}} = 0.1$ nm, $\Delta n_a = 0.01$, and $\Delta\lambda_{\text{peak}} = 46$ nm, the calculated maximum sensor resolution is 2.17×10^{-5} RIU. Moreover, the proposed sensor shows average wavelength sensitivities of 2760 and 2880 nm/RIU over the entire analyte RI range in

TABLE I
PERFORMANCE ANALYSIS BY VARYING ANALYTE REFRACTIVE INDEX FROM 1.33 TO 1.38

| Analyte RI	Analyte RI difference	Polarization mode	Peak loss (dB/cm)	Res. peak wavelength (nm)	Res. peak shift (nm)	Wavelength Sensitivity (nm/RIU)	Wavelength resolution (RIU)
1.33	0.01	x-polarization	0.503	580	20	2000	5×10^{-5}
		y-polarization	4.048	580	20	2000	5×10^{-5}
1.34	0.01	x-polarization	0.653	600	20	2000	5×10^{-5}
		y-polarization	5.399	600	20	2000	5×10^{-5}
1.35	0.01	x-polarization	0.853	620	25	2500	4×10^{-5}
		y-polarization	7.203	620	25	2500	4×10^{-5}
1.36	0.01	x-polarization	1.151	645	30	3000	3.33×10^{-5}
		y-polarization	9.889	645	33	3300	3.03×10^{-5}
1.37	0.01	x-polarization	1.656	675	43	4300	2.32×10^{-5}
		y-polarization	14.33	678	46	4600	2.17×10^{-5}
1.38	0.01	x-polarization	2.578	718	N/A	N/A	N/A
		y-polarization	22.632	724	N/A	N/A	N/A
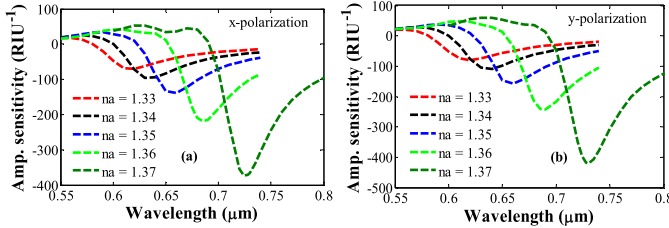
Fig. 4. Amplitude sensitivity with the variation of analyte RI from 1.33 to 1.37 for (a) x-polarized mode and (b) y-polarized mode. The fiber design parameters are set to: $\Lambda = 2$ μm, $d_c = 0.4$ μm, $d_1 = 0.6$ μm, $d = 1.3$ μm and $t_g = 30$ nm.

x- and y-polarized mode, respectively. In this case, the calculated wavelength resolutions are 3.62×10^{-5} RIU and 3.47×10^{-5} RIU, respectively. Note that during the calculation of sensor resolution, the influence of noise has been not considered. Table 1 shows the complete performance comparison of the proposed biosensor showing the variation of analyte RI from 1.33 to 1.38 in both x- and y-polarized modes. In this case, the gold layer thickness of 30 nm is considered.

Since the wavelength interrogation method provides sensitivity at a specific wavelength only, its implementation is costly. On other hand, amplitude sensitivity is simple and cost effective because it does not require wavelength interpolation. The amplitude sensitivity of the proposed sensor can be obtained from [22],

$$S_A(\text{RIU}^{-1}) = -\frac{1}{\alpha(\lambda, n_a)} \frac{\partial \alpha(\lambda, n_a)}{\partial n_a} \quad (5)$$

where $\alpha(\lambda, n_a)$ is the confinement loss at refractive index of n_a and $\partial \alpha(\lambda, n_a)$ is the confinement loss difference due to two adjacent analyte RIs.

Amplitude sensitivity of the proposed sensor for x- and y-polarized modes are shown in Fig. 4(a) and (b), while analyte RI is changed from 1.33 to 1.37. It can be evident from the figure that amplitude sensitivity increases drastically with the increment of analyte RI. According to Fig. 4, maximum amplitude sensitivity of 371.5 and 420.4 RIU^{-1} can be achieved with analyte RI of 1.37 in x- and y-polarized

modes, respectively. These sensitivities have been obtained at the wavelength of 0.718 and 0.724 μm, respectively.

The proposed sensor shows amplitude sensitivity of 72, 95, 140, 220 and 371.5 RIU^{-1} in x-polarized mode. Additionally, amplitude sensitivities of 76, 108, 157, 243 and 420.4 RIU^{-1} are obtained in y-polarized mode with the same analyte RI.

Using the amplitude interrogation method, the maximum sensor resolution has been obtained at analyte RI of 1.37, which is 2.69×10^{-5} and 2.37×10^{-5} RIU in x- and y-polarized mode, respectively. It should be noted that while calculated sensor resolution, it is assumed that minimum 1% transmitted intensity can be detected by the sensor. Using the same assumption, in x-polarized mode, sensor resolutions about 1.38×10^{-4}, 1.05×10^{-4}, 7.14×10^{-5}, 4.54×10^{-5} RIU are obtained at analyte RIs of 1.33, 1.34, 1.35 and 1.36, respectively. For y-polarized mode, the sensor resolutions are 1.31×10^{-4}, 9.25×10^{-5}, 6.36×10^{-5}, 4.11×10^{-5} RIU while the analyte RI are 1.33, 1.34, 1.35 and 1.36. The maximum sensor resolution is 2.37×10^{-5} RIU; therefore, the proposed sensor can be implemented for detecting smallest RI change order of 10^{-5}. The calculated sensor resolution is better than previously reported results [14], [15], [17], [19], [23], [24].

The variation of gold layer thickness has noticeable impact on the loss depth and amplitude sensitivity. The loss spectrum in x- and y-polarized mode with the variation of gold layer thickness at analyte RI of 1.36 is shown in Fig. 5. According to this figure, there is a noticeable reduction of loss depth with increasing the gold layer thickness. An identical scenario has been observed in both x- and y-polarized modes. The minimum loss depth has been found about 0.769 dB/cm and 7.14 dB/cm in x- and y-polarized modes at 0.77 and 0.775 μm, respectively. Due to the damping effect of gold layer, loss depth is decreased with increasing of gold layer thickness [23]. Another important fact can be noticed that increasing gold layer thickness results red shift. This is true for both x- and y-polarized modes.

Amplitude sensitivity of the proposed biosensor for the variation of the gold layer thickness in both x- and y-polarized mode is depicted in Fig. 6 (a) and (b). As illustrated in the
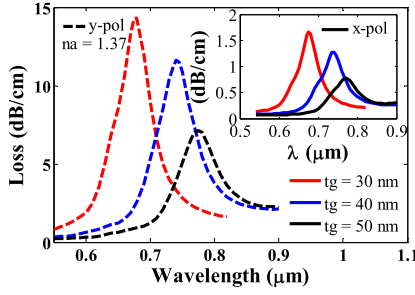
Fig. 5. Loss spectrum with the variation of gold layer thickness in x- and y-polarized modes. The fiber design parameters are set to: $\Lambda = 2$ μm, $d_c = 0.4$ μm, $d_1 = 0.6$ μm, $d = 1.3$ μm and $n_a = 1.36$.
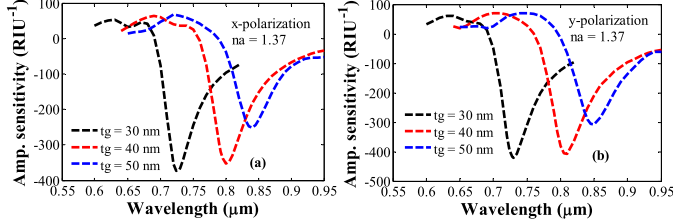

Fig. 6. Amplitude sensitivity with the variation of gold layer thickness in (a) x-polarized and (b) y-polarized mode. The fiber design parameters are set to: $\Lambda = 2$ μm, $d_c = 0.4$ μm, $d_1 = 0.6$ μm, $d = 1.3$ μm and $n_a = 1.37$.
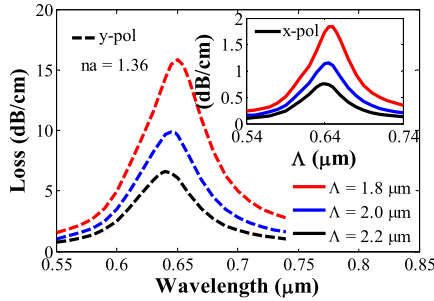

Fig. 7. Loss spectrum with the variation pitch from 1.8 to 2.2 μm in x- and y-polarized modes. The fiber design parameters are set to: $d_c = 0.4$ μm, $d_1 = 0.6$ μm, $d = 1.3$ μm, $t_g = 30$ nm and $n_a = 1.36$.

figure, in both x- and y-polarized modes, amplitude sensitivity reduces with increasing of gold layer thickness. In Fig. 5, it has demonstrated that incrementing gold thickness leads to decrease of the loss depth. Due to such reduction of loss depth, the evanescent field weakly interacts with the analyte, resulting in reduction of the amplitude sensitivity. The designed sensor exhibits maximum amplitude sensitivities of 371.5, 349 and 251 RIU^{-1} in x-polarized mode with gold layer thickness of 30, 40 and 50 nm, respectively. Additionally, with the same gold layer thickness maximum amplitude sensitivities of 420.4, 407, 307 RIU^{-1} have been obtained in y-polarized mode.

Fig. 7 shows the loss spectrum of the proposed biosensor considering the variation of pitch from 1.8 to 2.2 μm. As observed in the figure, scaling up the pitch value causes significant reduction of the loss depth in both x- and y-polarized modes. When pitch is increased, the difference of n_{eff} between core and cladding increases; therefore, loss depth is noticeably reduced. The maximum loss depth has been found about 1.84 and 15.85 dB/cm in x- and y-polarized mode, while pitch value is 1.8 μm with analyte RI of 1.36. According to the figure, in both x- and y-polarized modes, a small blue shift has been observed. The resonance wavelength shifts
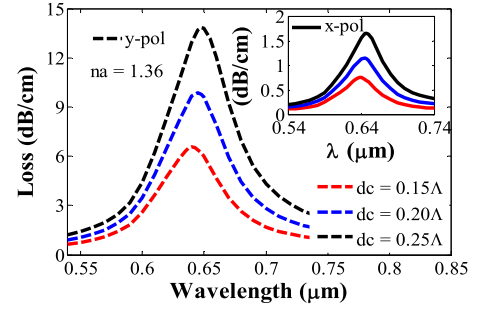

Fig. 8. Loss spectrum with the variation of central air hole diameter from 0.15Λ to 0.25Λ in x- and y-polarized modes. The fiber design parameters are set to: $\Lambda = 2$ μm, $d_1 = 0.6$ μm, $d = 1.3$ μm, $t_g = 30$ nm and $n_a = 1.36$.
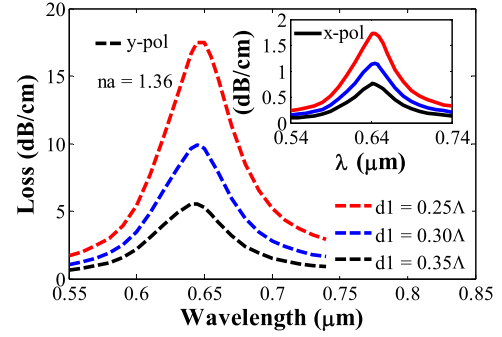
Fig. 9. Loss spectrum with the variation of d_1 from 0.25Λ to 0.35Λ in x- and y-polarized modes. The fiber design parameters are set to: $\Lambda = 2$ μm, $d_c = 0.4$ μm, $d = 1.3$ μm, $t_g = 30$ nm and $n_a = 1.36$.

from 0.65 to 0.645 μm and 0.645 to 0.64 μm when pitch is changed from 1.8 to 2 μm and 2 to 2.2 μm. An identical scenario has been obtained in both x- and y-polarized mode.

The effect of changing central air hole diameter (d_c) on the loss spectrum is illustrated in Fig. 8. It is evident from the figure that higher loss depth can be obtained by scaling up the value of d_c. With larger d_c, the n_{eff} difference between core and cladding gets smaller. As a result, loss of the proposed sensor increases. The maximum loss depth of 1.65 and 13.83 dB/cm has been found in x- and y-polarized modes with $d_c = 0.25\Lambda$. A close observation in the same figure indicates that there is small red shift when d_c is enlarged. The resonant wavelength shifts from 0.64 to 0.645 μm and 0.645 to 0.648 μm when d_c is changed from 0.15Λ to 0.2Λ and 0.20Λ to 0.25Λ μm, respectively. The exactly same scenario has been obtained in both x- and y-polarized mode.

Fig. 9 shows the loss spectrum of the proposed sensor when d_1 is varied from 0.25Λ to 0.35Λ in x- and y-polarized modes, respectively. It can be noticed that there is a noticeable impact on the loss spectrum with the variation of d_1. When d_1 is increased from 0.25Λ to 0.35Λ, the loss depth decreases to 1.73 to 0.75 dB/cm and 17.46 to 5.54 dB/cm in x- and y-polarized modes, respectively. Additionally, small blue shift has been found with the increasing of d_1. The resonant wavelength shifts from 0.65 to 0.645 μm and 0.645 to 0.642 μm when d_1 is changed from 0.25Λ to 0.3Λ and 0.3Λ to 0.35Λ. Both x- and y-polarized modes show the identical resonant wavelength shifting characteristics.

A linear fitting characteristic is important for optimization of the sensor in a defined dynamic range. High sensor linearity

TABLE II

PERFORMANCE COMPARISON OF THE PROPOSED SENSOR WITH EXISTING SENSORS IN THE LITERATURE

| Ref.	Structure Type	Wavelength sensitivity (nm/RIU)	Resolution (wavelength inter.), (RIU)	Amplitude sensitivity (RIU^{-1})	Resolution (amplitude inter.), (RIU)	Detection RI range
[14]	Birefringent PCF sensor	2000	5×10^{-5}	317	3.15×10^{-5}	1.33–1.35
[15]	Multi-hole PCF sensor	2000	5×10^{-5}	370	2.70×10^{-5}	1.33–1.35
[19]	D-shaped PCF sensor	2520	3.96×10^{-5}	44	2.27×10^{-4}	1.33–1.35
[23]	Gold coated PCF sensor	4000	2.5×10^{-5}	320	3.12×10^{-5}	1.33–1.37
[29]	PCF interferometer	326	5.20×10^{-5}	—	—	1.33–1.44
[31]	Surface-core fibers	40	2.5×10^{-4}	—	—	1.333–1.461
[32]	Microstructured-core PCF	8500	2.02×10^{-6}	—	—	1.33–1.44
This work	Gold coated spiral PCF sensor	4300 (*x*-pol)	2.32×10^{-5}	371.5 (*x*-pol)	2.69×10^{-5} (*x*-pol)	1.33–1.38
		4600 (*y*-pol)	2.17×10^{-5}	420.4 (*y*-pol)	2.37×10^{-5} (*y*-pol)	1.33–1.38
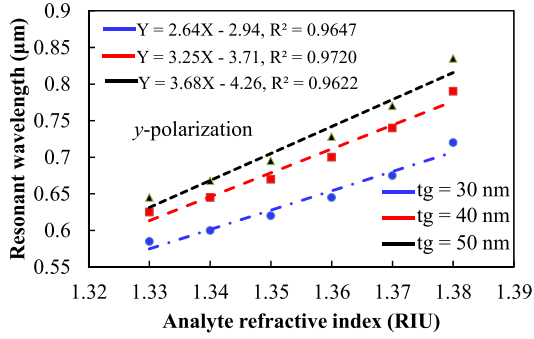
Fig. 10. Linear fitting with the variation of gold layer thickness in the *y*-polarized mode.

is a prerequisite for calibration sensors, especially for high RI analytes [14]. Moreover, the slope of the linear fitting curve represents the average sensitivity of a sensor. Nonlinearity of the response is not desired, as it causes significant variation of the average sensitivity and resolution that makes detection process complex. Linear fitting of the resonant wavelength with gold layer thickness of 30, 40 and 50 nm is depicted in Fig. 10. Here, the markers represent the resonant wavelengths and the solid lines represent the linear fitting. In a fitted regression line, R^2 value represents the degree of linear relationship between resonance wavelength and analyte RI. The R^2 value close to unity indicates near-ideal linearity. In the range of $1.33 \leq n_a \leq 1.38$, the proposed sensor shows adjusted R^2 value of 0.9647, 0.9720 and 0.9622 with gold layer thickness of 30, 40 and 50 nm, respectively. The corresponding regression equations are also given inside the figure. It should be mentioned only *y*-polarized mode is shown since *x*-polarized mode shows same results as obtained.

Due to high adjusted R^2 value, the proposed spiral PCF sensor can be potentially employed in practical sensing application.

Table II shows the comparison of the properties of the proposed sensor with existing designs in the literature. As seen from the table, the proposed sensor shows better performance in terms of sensitivity and sensor resolution. Moreover, detection range is also comparable with other SPR based sensors. Spiral PCF shows excellent modal properties that enable to control the sensitivity. The air holes of the spiral PCF are positioned in such a way that direct the evanescent field towards surface of the PCF. Therefore, the proposed spiral PCF sensor shows higher sensitivity than other configurations.

Fabrication of the proposed sensor is a key issue when it comes to realize it in practical form. It has been already demonstrated that equiangular spiral PCF can be practically realized by employing the stack and draw technique [33]. The target design can be obtained by exploiting a stacking method based on hexagonal close packing.

The complete fabrication recipe to realize the spiral PCF is discussed in [36]. In practice, to maintain a uniform coating of the thin gold layer is challenging. Chemical vapour deposition (CVD) [37] is an effective process that provides very smooth surface of the thin nanolayer. Besides, the newly reported gold atomic layer deposition (ALD) method can potentially be used [39], which can deposit a uniform gold coating on the curved fiber surface.

IV. CONCLUSION

In summary, we propose a dual-polarized spiral PCF based SPR sensor. Plasmonic gold metal is used to obtain sharp resonance peak and is placed on the outer surface of the PCF to facilitate ease of fabrication. Thorough analysis of the designed sensor shows that in the RI sensing range from 1.33 to 1.38, it is possible to obtain wavelength sensitivity of 4600 nm/RIU and amplitude sensitivity of 420.4 RIU^{-1} in the *y*-polarized mode. In the *x*-polarized mode, the maximum

wavelength sensitivity is 4300 nm/RIU and amplitude sensitivity is 371.5 RIU^{-1}. Moreover, the proposed sensor shows minimum loss of 0.403 and 4.048 dB/cm in *x*- and *y*-polarized modes, which indicates small length requirement of the PCF. Due to small size and promising sensing properties, the proposed sensor can be potentially implemented as an integrated SPR sensor in a lab-on-a-fiber chip.

REFERENCES

[1] S. Fang, H. J. Lee, A. W. Wark, and R. M. Corn, "Attomole microarray detection of MicroRNAs by nanoparticle-amplified SPR imaging measurements of surface polyadenylation reactions," *J. Amer. Chem. Soc.*, vol. 128, no. 43, pp. 14044–14046, Nov. 2006.

[2] I. Stemmler, A. Brecht, and G. Gauglitz, "Compact surface plasmon resonance-transducers with spectral readout for biosensing applications," *Sens. Actuator B, Chem.*, vol. 54, nos. 1–2, pp. 98–105, Jan. 1999.

[3] J. Homola, "Surface plasmon resonance sensors for detection of chemical and biological species," *Chem. Rev.*, vol. 108, no. 2, pp. 462–493, 2008.

[4] V. Koubová *et al.*, "Detection of foodborne pathogens using surface plasmon resonance biosensors," *Sens. Actuator B, Chem.*, vol. 74, nos. 1–3, pp. 100–105, Apr. 2001.

[5] A. Nooke *et al.*, "On the application of gold based SPR sensors for the detection of hazardous gases," *Sens. Actuator B, Chem.*, vol. 149, no. 1, pp. 194–198, Aug. 2010.

[6] P. J. Kajenski, "Tunable optical filter using long-range surface plasmons," *Opt. Eng.*, vol. 36, no. 5, pp. 1537–1541, May 1997.

[7] T. Akimoto, S. Sasaki, K. Ikebukuro, and I. Karube, "Refractive-index and thickness sensitivity in surface plasmon resonance spectroscopy," *Appl. Opt.*, vol. 38, no. 19, pp. 4058–4064, Aug. 1999.

[8] R. H. Ritchie, "Plasma losses by fast electrons in thin films," *Phys. Rev.*, vol. 106, no. 5, pp. 874–881, Jun. 1957.

[9] A. Otto, "Excitation of nonradiative surface plasma waves in silver by the method of frustrated total reflection," *Zeitschrift Phys.*, vol. 216, pp. 398–410, Aug. 1968.

[10] E. Kretschmann, "Radiative decay of non radiative surface plasmons excited by light," *Zeitschrift Naturforschung A*, vol. 23, no. 12, pp. 2135–2136, Dec. 1968.

[11] A. A. Rifat, M. R. Hasan, R. Ahmed, and H. Butt, "Photonic crystal fiber-based plasmonic biosensor with external sensing approach," *J. Nanophoton.*, vol. 12, no. 1, p. 012503, Jun. 2017.

[12] R. Otupiri, E. K. Akowuah, and S. Haxha, "Multi-channel SPR biosensor based on PCF for multi-analyte sensing applications," *Opt. Exp.*, vol. 23, no. 12, pp. 15716–15727, Jun. 2015.

[13] T. Wieduwilt *et al.*, "Ultrathin niobium nanofilms on fiber optical tapers—A new route towards low-loss hybrid plasmonic modes," *Sci. Rep.*, vol. 5, p. 17060, Nov. 2015.

[14] R. Otupiri, E. K. Akowuah, S. Haxha, H. Ademgil, F. AbdelMalek, and A. Aggoun, "A novel birefrigent photonic crystal fiber surface plasmon resonance biosensor," *IEEE Photon. J.*, vol. 6, no. 4, Aug. 2014, Art. no. 6801711.

[15] D. Gao, C. Guan, Y. Wen, X. Zhong, and L. Yuan, "Multi-hole fiber based surface plasmon resonance sensor operated at near-infrared wavelengths," *Opt. Commun.*, vol. 313, pp. 94–98, Feb. 2014.

[16] Z. Fan *et al.*, "High sensitivity of refractive index sensor based on analyte-filled photonic crystal fiber with surface plasmon resonance," *IEEE Photon. J.*, vol. 7, no. 3, Jun. 2015, Art. no. 4800809.

[17] J. N. Dash and R. Jha, "SPR biosensor based on polymer PCF coated with conducting metal oxide," *IEEE Photon. Technol. Lett.*, vol. 26, no. 6, pp. 595–598, Mar. 15, 2014.

[18] N. Luan, R. Wang, W. Lv, and J. Yao, "Surface plasmon resonance sensor based on D-shaped microstructured optical fiber with hollow core," *Opt. Exp.*, vol. 23, no. 7, pp. 8576–8582, Mar. 2015.

[19] X. Yang, Y. Lu, B. Liu, and J. Yao, "Analysis of graphene-based photonic crystal fiber sensor using birefringence and surface plasmon resonance," *Plasmonics*, vol. 12, no. 2, pp. 489–496, 2017.

[20] L. Peng, F. Shi, G. Zhou, S. Ge, Z. Hou, and C. Xia, "A surface plasmon biosensor based on a D-shaped microstructured optical fiber with rectangular lattice," *IEEE Photon. J.*, vol. 7, no. 5, Oct. 2015, Art. no. 4801309.

[21] A. A. Rifat *et al.*, "Copper-graphene-based photonic crystal fiber plasmonic biosensor," *IEEE Photon. J.*, vol. 8, no. 1, Feb. 2016, Art. no. 4800408.

[22] J. N. Dash and R. Jha, "Graphene-based birefringent photonic crystal fiber sensor using surface plasmon resonance," *IEEE Photon. Technol. Lett.*, vol. 26, no. 11, pp. 1092–1095, Jun. 1, 2014.

[23] A. A. Rifat *et al.*, "Surface plasmon resonance photonic crystal fiber biosensor: A practical sensing approach," *IEEE Photon. Technol. Lett.*, vol. 27, no. 15, pp. 1628–1631, Aug. 1, 2015.

[24] M. R. Hasan, S. Akter, A. A. Rifat, S. Rana, and S. Ali, "A highly sensitive gold-coated photonic crystal fiber biosensor based on surface plasmon resonance," *Photonics*, vol. 18, no. 4, p. 18, Mar. 2017.

[25] Y. Lu, X. Yang, M. Wang, and J. Yao, "Surface plasmon resonance sensor based on hollow-core PCFs filled with silver nanowires," *Electron. Lett.*, vol. 51, no. 21, pp. 1675–1677, Oct. 2015.

[26] S. I. Azzam, M. F. O. Hameed, R. E. A. Shehata, A. M. Heikal, and S. S. A. Obayya, "Multichannel photonic crystal fiber surface plasmon resonance based sensor," *Opt. Quantum Electron.*, vol. 48, p. 142, Feb. 2016.

[27] M.-C. Navarrete, N. Díaz-Herrera, A. González-Cano, and Ó. Esteban, "Surface plasmon resonance in the visible region in sensors based on tapered optical fibers," *Sens. Actuator B, Chem.*, vol. 190, pp. 881–885, Jan. 2014.

[28] A. A. Rifat *et al.*, "Highly sensitive multi-core flat fiber surface plasmon resonance refractive index sensor," *Opt. Exp.*, vol. 24, no. 3, pp. 2485–2495, Feb. 2016.

[29] J.-N. Wang and J.-L. Tang, "Photonic crystal fiber Mach-Zehnder interferometer for refractive index sensing," *Sensors*, vol. 12, no. 12, pp. 2983–2995, Mar. 2012.

[30] P. Torres, E. Reyes-Vera, A. Díez, and M. V. Andrés, "Two-core transversally chirped microstructured optical fiber refractive index sensor," *Opt. Lett.*, vol. 39, no. 6, pp. 1593–1596, Mar. 2014.

[31] J. H. Osório *et al.*, "Bragg gratings in surface-core fibers: Refractive index and directional curvature sensing," *Opt. Fiber Technol.*, vol. 34, pp. 86–90, Mar. 2017.

[32] B. Sun, M.-Y. Chen, Y.-K. Zhang, J.-C. Yang, J.-Q. Yao, and H.-X. Cui, "Microstructured-core photonic-crystal fiber for ultra-sensitive refractive index sensing," *Opt. Exp.*, vol. 19, no. 5, pp. 4091–4100, Feb. 2011.

[33] A. Vial, A.-S. Grimault, D. Macías, D. Barchiesi, and M. L. de la Chapelle, "Improved analytical fit of gold dispersion: Application to the modeling of extinction spectra with a finite-difference time-domain method," *Phys. Rev. B, Condens. Matter*, vol. 71, p. 085416, Feb. 2005.

[34] A. A. Rifat, R. Ahmed, G. A. Mahdiraji, and F. R. M. Adikan, "Highly sensitive D-shaped photonic crystal fiber-based plasmonic biosensor in visible to near-IR," *IEEE Sensors J.*, vol. 17, no. 9, pp. 2776–2783, May 2017.

[35] B. Shuai, L. Xia, Y. Zhang, and D. Liu, "A multi-core holey fiber based plasmonic sensor with large detection range and high linearity," *Opt. Exp.*, vol. 20, no. 6, pp. 5974–5986, Mar. 2012.

[36] A. Agrawal, Y. O. Azabi, and B. M. A. Rahman, "Stacking the equiangular spiral," *IEEE Photon. Technol. Lett.*, vol. 25, no. 3, pp. 291–294, Feb. 1, 2013.

[37] P. J. A. Sazio *et al.*, "Microstructured optical fibers as high-pressure microfluidic reactors," *Science*, vol. 311, no. 5767, pp. 1583–1586, 2006.

[38] M. B. E. Griffiths, P. J. Pallister, D. J. Mandia, and S. T. Barry, "Atomic layer deposition of gold metal," *Chem. Mater.*, vol. 28, no. 1, pp. 44–46, Jan. 2016.

Md. Rabiul Hasan, photograph and biography not available at the time of publication.

Sanjida Akter, photograph and biography not available at the time of publication.

Ahmmed A. Rifat, photograph and biography not available at the time of publication.

Sohel Rana, photograph and biography not available at the time of publication.

Kawsar Ahmed, photograph and biography not available at the time of publication.

Rajib Ahmed, photograph and biography not available at the time of publication.

Harish Subbaraman, photograph and biography not available at the time of publication.

Derek Abbott, photograph and biography not available at the time of publication.